

Safety-Aware Hybrid Control of Airborne Wind Energy Systems

Nikolaus Vertovec *

Department of Engineering Science, University of Oxford Parks Road, OX1 3PJ

Sina Ober-Blöbaum †

Department of Mathematics, Paderborn University, 33100

Kostas Margellos ‡

Department of Engineering Science, University of Oxford Parks Road, OX1 3PJ

A fundamental concern in progressing Airborne Wind Energy (AWE) operations towards commercial success, is guaranteeing that safety requirements placed on the systems are met. Due to the high dimensional complexity of AWE systems, however, formal mathematical robustness guarantees become difficult to compute. We draw on research from Hamilton-Jacobi (HJ) reachability analysis to compute the optimal control policy for tracking a flight path, while enforcing safety constraints on the system. In addition, the zero-sublevel set of the computed value function inherent in HJ reachability analysis indicates the backward reachable set, the set of states from which it is possible to safely drive the system into a target set within a given time without entering undesirable states. Furthermore, we derive a switching law, such that the safety controller can be used in conjunction with arbitrary least restrictive controllers to provide a safe hybrid control law. In such a setup, the safety controller is only activated when the system approaches the boundary of its maneuverability envelope. Such a hybrid control law is a notable improvement over existing robust control approaches that deteriorate performance by assuming the worst-case environmental and system behavior at all times. We illustrate our results via extensive simulation-based studies.

I. Introduction

With the looming threat of the climate crisis becoming ever more detrimental, the need for low-cost and reliable sources of energy becomes increasingly pressing. Wind remains the primary non-hydro renewable and to reach net-zero energy targets of 8008 TWh in 2030, will need to grow annually by 18% between 2021 and 2030 [1]. Conventional wind turbines have high material costs and often struggle with unreliable wind patterns present at low altitudes. Airborne Wind Energy (AWE) systems solve many of the problems of conventional wind turbines by harnessing wind energy at high altitudes, where stronger and more reliable wind currents can be found. Thus, over the past decade, we have seen a

*Doctoral Student, Department of Engineering Science, University of Oxford; nikolaus.vertovec@eng.ox.ac.uk.

†Professor, Department of Mathematics, Paderborn University, 33100; sinaober@math.uni-paderborn.de

‡Associate Professor, Department of Engineering Science, University of Oxford; kostas.margellos@eng.ox.ac.uk

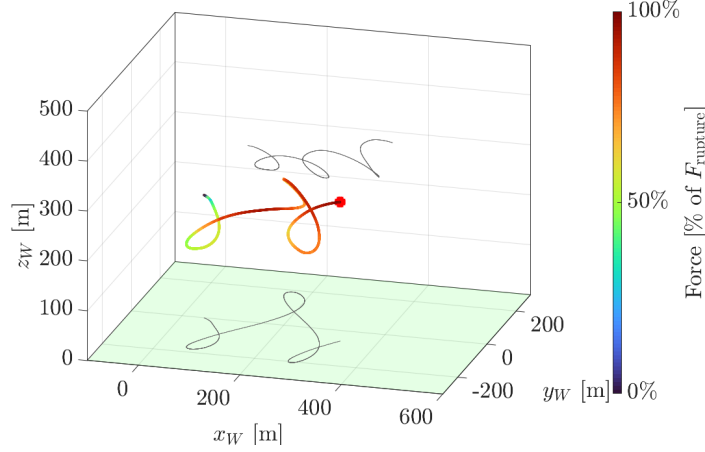


Fig. 1 Tether rupture during traction phase of flight. The red dot marks the point during flight at which a tether rupture occurs due to the maximum tether force being exceeded.

rapid increase in research and development into AWE from both academia and the private sector [2, 3].

In this paper, we only consider Ground-Gen systems, whereby energy is obtained by continuously performing two phases of flight, a *traction* phase, and a *retraction* phase. During the traction phase, a tethered kite or fixed-wing aircraft is flown in crosswind conditions at altitudes of up to 1000m above ground. The traction force acting on the aircraft's tether is converted into electricity using a generator and winch located at the base of the tether [4, 5]. For a discussion of alternative AWE systems, we refer to [5, 6]. Since the tether is gradually reeled out during the traction phase, the system will eventually need to be reset. For this, the aircraft is flown back to its starting altitude upwind in a phase commonly referred to as the retraction phase. During the retraction phase, a small amount of the previously generated energy needs to be spent on reeling in the tether. Nevertheless, AWE systems have been shown to be able to create a net energy output of over 20 kW [5] with proposed larger systems producing energy in the range of MWs [7].

For AWE systems to become widely adopted, it is necessary to provide formal guarantees on the state operation and control of such systems. The aim of this paper is to ensure robustness in the sense of safety-aware control of an AWE system with minimal impact on power generation. To this end, we propose a hybrid control law, whereby a safety controller is only activated when a critical system failure is predicted to occur. We consider an AWE setup as proposed in [8], whereby a fixed-wing aircraft is flown in a figure of eight flight pattern, controlled using nonlinear dynamic inversion (NDI), a control strategy common in aviation applications. The tether configuration is changed from [8], such that a tether rupture is deemed to occur when a maximum tether force of 1.87 kN is exceeded. As can be seen in Figure 1, the tether ruptures before the aircraft can complete one full cycle of flight. Using Hamilton Jacobi (HJ) reachability analysis, we will synthesize a safety controller as well as switching conditions, such that in a hybrid control setup, minimal penalties on power generation are incurred, while ensuring a safe flight without tether rupture.

HJ reachability analysis has become a well-adopted formal verification method, whereby the optimal controller is

derived through computation of the backward reachable set (BRS). Its advantages include compatibility with nonlinear system dynamics, formal treatment of nonlinear bounds, and recently also with multi-objective optimization problems [9, 10]. However, since HJ reachability analysis requires solving a quasi-variational inequality over a gridded state space, it is subject to the curse of dimensionality. As such, its applications have been limited to low-dimensional systems [11].

To this end, we will derive a novel low-dimensional formulation of the system dynamics of AWE systems and formulate the safety critical control problem as a differential game of two players. Furthermore, for numerical reasons that will become evident later on, we are required to grid the state space, thus necessitating a coordinate transformation that ensures only relevant states are considered for controller synthesis, minimizing numerical overhead. Thus the key contributions of this paper are

- 1) the development of a simplified low dimensional AWE model that is accurate enough for safety-critical control purposes (Section III),
- 2) the synthesis and deployment of the safety-critical controller based on the developed abstractions and HJ reachability analysis, a non-trivial application for which we have made the code and simulation environment available (Section IV),
- 3) the computation of the optimal control/disturbance actions that optimize the Hamiltonian of the underlying optimal control problem, which is case-dependent and non-trivial in the setting (Section IV.B).
- 4) the validation of the performance of the controller by applying it to a high fidelity model, thus rendering our controller as an add-on to existing tools to guarantee safety (Section V).

The remainder of the paper is organized as follows: Section II discusses the AWE model used for simulation purposes as well as the guidance strategy and baseline controller. Section III introduces the simplifications, abstractions, and the new reference frame used to derive a low dimensional model of the AWE system suitable for safety-control synthesis, with the safety controller being derived and introduced in Section IV. Finally, in Section V we validate the controller in its hybrid control setup using the high fidelity AWE model and discuss the effects on power generation with Section VI providing concluding remarks and directions of future research.

II. Modeling

The modeling of AWE systems has been well studied and a variety of definitions for the equations of motion have been derived. Yet commonly AWE systems require a high number of states in order to accurately capture both the dynamics of the kite or aircraft as well as the tether and the associated winch controller. Since the goal of this paper is to derive a safety-critical controller for the AWE system using HJ reachability analysis, we seek the development of a simplified yet accurate enough, from a control point of view, model.

In the following section, we begin by modeling the AWE system based predominantly on the work of [8] with extensions taken from [12, 13] and [14]. This model will be used for simulation purposes in Section V and is presented

to provide the necessary notation and understanding needed for the abstractions and synthesis, the primary contributions of this work, in Sections III and IV.

A. Reference Frames

For the discussion of the dynamics of AWE systems, it is useful to introduce a variety of reference frames. The utilized reference frames (with the exception of the Γ frame, Section III.C) are common for AWE systems and have been extensively discussed in [8] and [15]. For the transformation from one reference frame to another, we introduce the transformation matrices $\mathbf{M}_{(\cdot)(\cdot)}$, where the first subscript indicates the destination frame and the second subscript indicates the origin frame. Thus, as an example, the kinematic velocity in the τ frame, where τ denotes one of the employed frames, can be obtained from the body fix frame (B) by $(\mathbf{v}_k)_\tau = \mathbf{M}_{\tau B}(\mathbf{v}_k)_B$. The transformation matrices for the reference frames are listed in the appendix. We utilize bold notation for vectors and matrices and regular notation for scalars. Furthermore, we utilize subscripts to denote vector elements, i.e., $(v_k)_{\tau,y}$ denotes the y component of the kinematic velocity in the τ frame.

1. Wind Frame

The wind frame (W) is a rotation of the commonly used North-East-Down (NED or O) frame. The x-axis of the W frame is aligned with the mean wind direction (denoted by ξ). We assume that the mean wind direction is such that the z-axis of the W frame points upwards and the y-axis forms a right-hand reference frame (Figure 2).

2. Tangential Frame

The tangential frame (τ) is centered at the position of the aircraft, such that the z-axis points towards the origin of the NED frame. To this end, the x-axis points towards the north direction, while the y-axis completes a right-hand reference frame. Since the τ frame moves together with the aircraft, its location is determined using the longitude (λ) and latitude (ϕ) as well as the distance to the origin (h_τ) (Figure 2).

3. Aerodynamic Frame

The aircraft's kinematic velocity is denoted by \mathbf{v}_k and is composed of the aerodynamic velocity \mathbf{v}_a as well as the wind velocity \mathbf{v}_w , i.e., $\mathbf{v}_k = \mathbf{v}_a + \mathbf{v}_w$. This relationship holds true regardless of reference frame. For a discussion of the aerodynamic velocity, we define the aerodynamic frame (A) such that the velocity vector \mathbf{v}_a is aligned with the x-axis. For the derivation with respect to the NED frame, we first rotate the NED frame by the course angle χ_a and path angle γ_a , resulting in the intermediate frame \bar{A} , before tilting the frame by the bank angle μ_a (Figure 2).

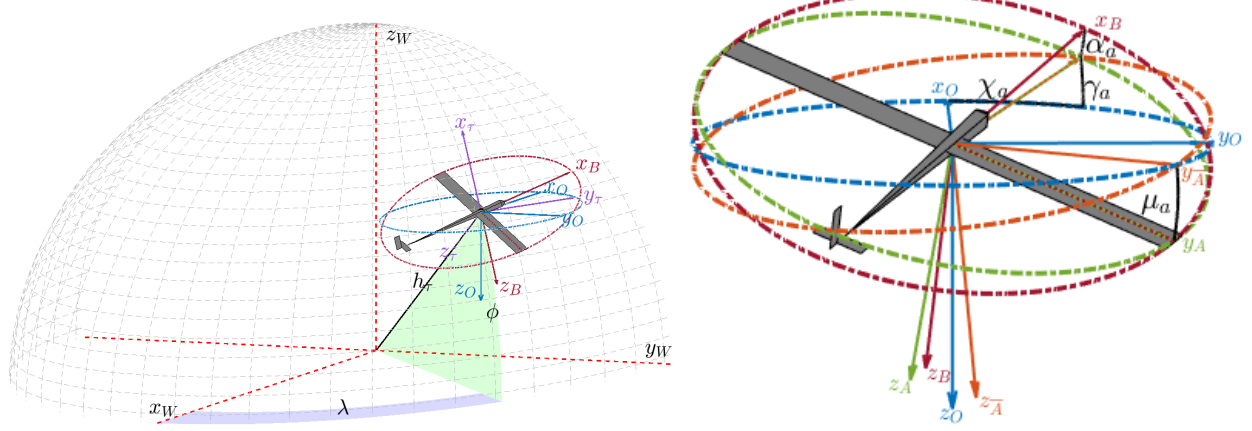


Fig. 2 Visualization of the reference frames. The NED frame is depicted in blue. The intermediate aerodynamic frame, \bar{A} , is a rotation of the NED (O) frame by the course angle χ_a and path angle γ_a and is depicted in orange. The aerodynamic frame, A, is achieved by further rotating the \bar{A} by μ_a and is depicted in green. The body frame, B, is depicted in red and is achieved by rotating the A frame by the angle of attack α_a , neglecting the sideslip angle β_a . Finally, the tangential frame is depicted in purple in relation to the wind frame.

4. Body-Fixed Frame

The body-fixed frame (B) is used to calculate the aerodynamic forces acting on the aircraft. It can be obtained from the aerodynamic frame using the angle of attack α_a as well as the sideslip angle β_a (Figure 2).

B. Aircraft Equations of Motion and Ground Station Model

For the AWE system considered in this paper, we simplify the modeling of the aircraft by neglecting the yaw, pitch, and roll rates as well as the sideslip angle β_a . As control inputs we consider the bank angle μ_a as well as the angle of attack α_a . A more complex model of the AWE system is outside of the scope of this paper.

The position of the aircraft is defined in the W frame by $[\lambda, \phi, h_\tau]$ and it moves with velocity v_a along the x-axis of the \bar{A} frame. To connect the \bar{A} frame with the NED frame, we add the course angle χ_a and path angle γ_a as additional states. To influence the heading of the aircraft, we utilize the bank angle μ_a and angle of attack α_a as inputs to the system and assume that the sideslip angle β_a is negligible, i.e., $\beta_a = 0$.

Therefore our initial set of states used are $[\lambda, \phi, h_\tau, v_a, \chi_a, \gamma_a] \in \mathbb{R}^6$. The position propagation can be calculated from the kinematic velocity in the τ frame as follows:

$$\dot{\lambda} = \frac{(v_k)_{\tau,y}}{\cos(\phi)h_\tau}, \quad (II.1)$$

$$\dot{\phi} = \frac{(v_k)_{\tau,x}}{h_\tau}, \quad (II.2)$$

$$\dot{h}_\tau = -(v_k)_{\tau,z}, \quad (II.3)$$

where $(v_k)_{\tau,x}$, $(v_k)_{\tau,y}$ and $(v_k)_{\tau,z}$ denote the x, y and z components of the kinematic velocity in the τ frame, respectively.

$(\mathbf{v}_k)_\tau$ is calculated by transforming the kinematic velocity from the O frame to the W frame, and then to the τ frame using the appropriate transformation matrix, \mathbf{M}_{WO} and $\mathbf{M}_{\tau W}$, respectively, found in the appendix. $(\mathbf{v}_k)_O$ is derived from the aerodynamic and wind velocity

$$(\mathbf{v}_k)_O = \mathbf{M}_{OA} \begin{bmatrix} v_a, 0, 0 \end{bmatrix}_A^T + (\mathbf{v}_W)_O. \quad (\text{II.4})$$

By assuming the wind field stays stationary, we are able to calculate the derivative of the kinematic velocity using the gravitational force (\mathbf{F}_g) , aerodynamic force (\mathbf{F}_a) , as well as the force the tether exerts on the aircraft (\mathbf{F}_t) . For a complete derivation we refer to [8].

$$\begin{bmatrix} \dot{v}_a \\ \dot{\chi}_a \\ \dot{\gamma}_a \end{bmatrix} = \frac{1}{m_a} \begin{bmatrix} 1 & 0 & 0 \\ 0 & \frac{1}{v_a \cos \gamma_a} & 0 \\ 0 & 0 & -\frac{1}{v_a} \end{bmatrix} \left(\mathbf{M}_{AO} [(\mathbf{F}_g)_O + (\mathbf{F}_t)_O] + \mathbf{M}_{AA} \mathbf{M}_{AB} (\mathbf{F}_a)_B \right), \quad (\text{II.5})$$

where m_a denotes the mass of the aircraft. Note that the matrix \mathbf{M}_{AO} depends on the course and path angles χ_a and γ_a , \mathbf{M}_{AA} depends on the bank angle μ_a and \mathbf{M}_{AB} depends on the angle of attack α_a and sideslip angle β_a .

1. Ground Station Model

The ground station serves as the power generator for the AWE system. The winch controller within the ground station is responsible for reeling out and reeling in the tether during flight. The winch is essentially a drum on which the tether is wound. The position of the drum is defined by θ_w and the reeled out tether length is simply calculated as $l_{\text{tether}} = r_w \theta_w$, where r_w is the drum radius. Using the same dynamics as in [13], we can thus describe the winch using a second order system.

$$\dot{\theta}_w = \omega_w, \quad (\text{II.6})$$

$$\dot{\omega}_w = \frac{1}{J_w} (r_w \|\mathbf{F}_w\|_2 - \nu_w \dot{\theta}_w + M_c), \quad (\text{II.7})$$

where ν_w is the friction coefficient, ω_w is the rotation rate of the drum, \mathbf{F}_w is the tether force at the ground station (equal to $\mathbf{F}_{s,0}$ in II.B.3), and J_w is the inertia of the winch. For the control of the winch in the simulation study discussed in Section V, we regulate the control moment M_c using a PI-controller that attempts to track a given reference tether force, F_{ref} .

2. Gravitational and Aerodynamic Forces

The gravitational force can simply be expressed in the O frame as

$$(\mathbf{F}_g)_O = \begin{bmatrix} 0, & 0, & m_a g \end{bmatrix}^T \in \mathbb{R}^3, \quad (\text{II.8})$$

where g is the gravitational constant. As mentioned earlier, we assume yaw, pitch and roll rates to be zero and neglect the effects of the sideslip angle β_a . This simplifies the aerodynamic coefficients derived in [12], to

$$\begin{bmatrix} C_x \\ C_y \\ C_z \end{bmatrix} = \begin{bmatrix} C_{x,0}(\alpha_a) + C_{x,\delta_e}(\alpha_a)\delta_e \\ C_{y,\delta_a}(\alpha_a)\delta_a + C_{y,\delta_r}(\alpha_a)\delta_r \\ C_{z,0}(\alpha_a) + C_{z,\delta_e}(\alpha_a)\delta_e \end{bmatrix}, \quad (\text{II.9})$$

where we consider the aileron (δ_a), elevator (δ_e) and rudder (δ_r) deflections to be constant and all α_a dependent coefficients are approximated using second order polynomials. Using the aerodynamic coefficients we can then calculate the aerodynamic force of the aircraft as

$$(\mathbf{F}_a)_B = \frac{1}{2} \rho S_{\text{ref}} v_a^2 \begin{bmatrix} C_x, & C_y, & C_z \end{bmatrix}^T, \quad (\text{II.10})$$

where S_{ref} is the aerodynamic reference area corresponding to the projected surface area of the aircraft wing [12], and ρ is the air density.

3. Tether Forces

For the calculation of the tether forces (\mathbf{F}_t) that act on the aircraft, we use models of varying complexity. For the controllers, we rely on a straight tether approximation, whereas for simulation purposes, we use a tether model similar to the model derived in [14]. We begin by deriving the most complex of the three tether models employed in this paper.

Let us first consider a fixed number of lumped masses connected by n spring-damper elements. The length of each segment is denoted by l_s and the spring and damping constants for each segment are denoted by k and c , respectively. Each tether segment is modeled as a point mass with position \mathbf{p}_i and velocity \mathbf{v}_i , as shown in Figure 3. The equations of motion of the tether segment are given by

$$\dot{\mathbf{p}}_i = \mathbf{v}_i, \quad (\text{II.11})$$

$$\dot{\mathbf{v}}_i = m_i^{-1} \mathbf{F}_i, \quad (\text{II.12})$$

where m_i is the mass of an individual segment and \mathbf{F}_i is the tether segment force. The tether segment force for segment

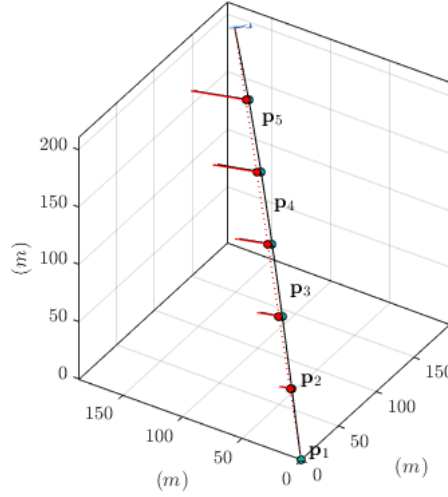


Fig. 3 Visualization of the tether modeled as a straight tether (red) and as a fixed number of lumped masses (blue). The velocities of the point masses are shown by the red and blue vectors respectively.

i is given by

$$\mathbf{F}_i = \mathbf{F}_{s,i+1} - \mathbf{F}_{s,i} - \mathbf{F}_{g,s} + \mathbf{F}_{a,i}, \quad (\text{II.13})$$

where $\mathbf{F}_{g,s}$ is the gravitational force acting on the tether segment, $\mathbf{F}_{a,i}$ is the aerodynamic drag acting on the i-th segment, and $\mathbf{F}_{s,i}$ is the tensile force of the i-th segment.

The tensile force is calculated according to Hooke's law

$$\mathbf{F}_{s,i} = \left(k(\|\mathbf{s}_i\|_2 - l_s) + c\left(\frac{\mathbf{s}_i}{\|\mathbf{s}_i\|_2} \mathbf{s}_{v,i}\right) \right) \frac{\mathbf{s}_i}{\|\mathbf{s}_i\|_2}, \quad (\text{II.14})$$

where $\mathbf{s}_i = \mathbf{p}_i - \mathbf{p}_{i-1}$ and $\mathbf{s}_{v,i} = \mathbf{v}_i - \mathbf{v}_{i-1}$. Thus the maximum tether force is exerted on the final segment attached to the aircraft, i.e., $\mathbf{F}_t = \mathbf{F}_{s,n+1}$, with $\mathbf{s}_{n+1} = \mathbf{p}_{\text{aircraft}} - \mathbf{p}_n$ and $\mathbf{s}_{v,n+1} = \mathbf{v}_{\text{aircraft}} - \mathbf{v}_n$ and $\mathbf{p}_{\text{aircraft}}$ and $\mathbf{v}_{\text{aircraft}}$ are the position and velocity, respectively, of the aircraft in Cartesian coordinates.

For the tether drag calculation, we begin by introducing the apparent air velocity, $\mathbf{v}_{a,i}$, composed of the wind speed at the height of the i-th particle ($\mathbf{v}_{w,i}$), as well as the average segment velocity

$$\mathbf{v}_{a,i} = \mathbf{v}_{w,i} - \frac{\mathbf{v}_{i+1} + \mathbf{v}_i}{2}. \quad (\text{II.15})$$

Each segment is modeled as a cylinder, thus the drag is caused predominantly by the velocity perpendicular to the tether segment

$$\mathbf{v}_{a,i,\perp} = \mathbf{v}_{a,i} - \left(\frac{\mathbf{s}_i^T \mathbf{v}_{a,i}}{\|\mathbf{s}_i\|_2} \right) \frac{\mathbf{s}_i}{\|\mathbf{s}_i\|_2}. \quad (\text{II.16})$$

Using the perpendicular velocity components, the final tether drag is given by

$$\mathbf{F}_{a,i} = \frac{1}{2} \rho C_{d,t} \mathbf{v}_{a,i,\perp} \|\mathbf{v}_{a,i,\perp}\|_2 A_{\text{eff},t}, \quad (\text{II.17})$$

where $C_{d,t}$ is the tether drag coefficient and $A_{\text{eff},t}$ is the projected tether area perpendicular to $\mathbf{v}_{a,i}$,

$$A_{\text{eff},t} = d_t \|\mathbf{s}_i - \mathbf{s}_i \frac{\mathbf{v}_{a,i}}{\|\mathbf{v}_{a,i}\|_2}\|_2, \quad (\text{II.18})$$

where d_t is the tether diameter.

This complex tether model requires $6n$ additional states, where n is the number of segments used, and is therefore only suited for simulation purposes. For the controller synthesis we use two simplified tether models that rely on a straight tether approximation. Both models will be introduced in Section III.A and Section II.E.

4. Wind Field Model

To capture the varying wind speeds at different altitudes we employ the wind shear model provided by the MATLAB Aerospace Toolbox [16].

$$(\mathbf{v}_{\text{shear}})_O = W_{20} \frac{\ln(\frac{h}{z_0})}{\ln(\frac{20}{z_0})}, \quad (\text{II.19})$$

where h is the altitude of the aircraft in feet, z_0 is a constant equal to 0.15 feet, and W_{20} is the measured wind speed at an altitude of 20 feet.

In addition to the wind shear, we also model atmospheric turbulence in form of a continuous Dryden wind turbulence model. The Dryden model is a stochastic gust model, whereby the linear and angular velocities of the atmospheric turbulence are modeled as spatially varying stochastic processes, each with a specific power spectral density. The longitudinal, lateral, and vertical component spectra functions are provided by Military Handbook MIL-HDBK-1797B [17]. For the implementation of the Dryden model, we utilize the continuous Dryden model block provided by the MATLAB Aerospace Toolbox [16].

Neglecting the angular rates of the atmospheric turbulence and assuming the pitch, roll and yaw rates of the aircraft stay constant, the wind turbulence is given by $(\mathbf{v}_{\text{turb}})_W = [u_g, v_g, w_g]^T \in \mathbb{R}^3$, where u_g is the longitudinal turbulence velocity aligned along the horizontal relative mean wind vector, v_g is the lateral turbulence velocity and w_g is the vertical turbulence velocity. Due to the varying altitudes of the aircraft, the terms u_g , v_g and w_g are computed by passing a band-limited white noise signal through two sets of forming filters, one for low altitudes and one for high altitudes, and then interpolating the results.

Finally the wind velocity acting on the aircraft is computed by adding the turbulence to the wind shear $(\mathbf{v}_W)_O = (\mathbf{v}_{\text{turb}})_O + (\mathbf{v}_{\text{shear}})_O$.

C. Optimal Flight Path

The fundamental idea behind Ground-Gen AWE is to transfer the force from the aerodynamic lift of the aircraft or kite to the connected tether [18]. Similar to the blades of a wind turbine, this can be done by moving the aircraft perpendicular to the mean wind direction. To this end, it has become common practice in the AWE community to adopt a figure eight flight pattern. We thus use a Lissajous curve, Γ , lying on a sphere as the reference flight path. The two-dimensional curve can be described by its longitude λ_Γ and latitude ϕ_Γ . We parameterize Γ on \mathbb{S}^2 using the arc length s . In Cartesian coordinates the curve is then given by

$$\Gamma_P(s) = \begin{bmatrix} \cos \lambda_\Gamma(s) \cos \phi_\Gamma(s) \\ \sin \lambda_\Gamma(s) \cos \phi_\Gamma(s) \\ \sin \phi_\Gamma(s) \end{bmatrix} h_\tau. \quad (\text{II.20})$$

For the specific Lissajous curve, we opt for the Lemniscate of Booth [19], a commonly used figure eight curve, using the height/width ratio of $a_{\text{Booth}}/b_{\text{Booth}} = 120/200$. The longitude and latitude of the Lemniscate of Booth can be calculated as follows:

$$\lambda_\Gamma(s) = \frac{1}{h_\tau} \frac{b_{\text{Booth}} \sin s}{1 + \left(\frac{a_{\text{Booth}}}{b_{\text{Booth}}}\right)^2 \cos^2 s}, \quad (\text{II.21})$$

$$\phi_\Gamma(s) = \frac{1}{h_\tau} \frac{a_{\text{Booth}} \sin s \cos s}{1 + \left(\frac{a_{\text{Booth}}}{b_{\text{Booth}}}\right)^2 \cos^2 s}. \quad (\text{II.22})$$

We define our reference curve to lie centered on the horizon. However, during flight, we rotate the curve by ψ_0 to assist with power generation. Thus the tracking curve used during flight is given by

$$\Gamma(s, \psi_0) = \underbrace{\begin{bmatrix} \cos(\psi_0) & 0 & -\sin(\psi_0) \\ 0 & 1 & 0 \\ \sin(\psi_0) & 0 & \cos(\psi_0) \end{bmatrix}}_{\mathbf{M}_{\text{WP}}} \Gamma_P(s). \quad (\text{II.23})$$

Finally, the tangent of the curve is given by $\mathbf{t}(s) = \frac{d\Gamma}{ds} = \frac{\partial \Gamma}{\partial \lambda_\Gamma} \frac{\partial \lambda_\Gamma}{\partial s} + \frac{\partial \Gamma}{\partial \phi_\Gamma} \frac{\partial \phi_\Gamma}{\partial s}$.

D. Guidance Strategy

Since we only derive the safety controller for the traction phase, the most critical part of flight (neglecting take-off and landing), we refer to [8] for a complete discussion of the guidance strategy employed during retraction and transition from retraction to traction.

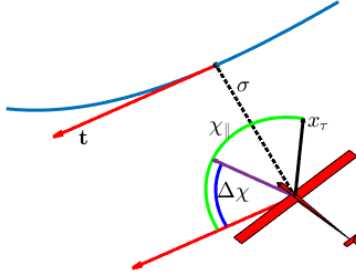


Fig. 4 Visualization of the guidance strategy to produce the optimal course heading (purple arrow).

As shown in Figure 7, the shortest path from the position of the aircraft (denoted by \mathbf{K}) to the closet point on the tracking curve (denoted by \mathbf{C}), is given by the geodesic vector σ . For perfect path tracking, we need to minimize $\|\sigma\|_2$. Taking the shortest path, however, would result in the aircraft intercepting the curve perpendicularly. In practice, this is not desirable and thus we need to introduce a commanded flight direction that results in the distance to the tracking curve being minimized, while also ensuring that when the aircraft intercepts the tracking curve, its kinematic velocity is aligned with the tangent of the curve, \mathbf{t} .

The commanded flight path can be defined on \mathbb{S}^2 , independently of the distance to the origin by simply scaling the parameters a_{Booth} and b_{Booth} by $1/h_\tau$. The optimal course angle $(\chi)_\tau$ should point the aircraft along the geodesic when far from the curve, however, point perpendicular to the geodesic to align with $\mathbf{t}(s)$ when close to the curve. We set the optimal flight path angle to zero to prevent the aircraft from going into a nose dive in order to quickly gain speed and reach the curve, something that would be counterintuitive to energy production.

To this end, let us define the optimal course and path angles as

$$(\gamma_{\text{cmd}})_\tau = 0, \quad (\text{II.24})$$

$$(\chi_{\text{cmd}})_\tau = (\chi_\parallel)_\tau + (\Delta\chi)_\tau, \quad (\text{II.25})$$

with $(\chi_\parallel)_\tau = \arctan \frac{t_y}{t_x}$, where t_x and t_y denote the x and y components of the curve tangent. The second component, $\Delta\chi_\tau$, of the command course angle ensures that as we approach the tracking curve, we align ourselves with the curve tangent \mathbf{t} . This is done by introducing a tuning parameter δ_0 , allowing us to calculate course change as

$$(\Delta\chi)_\tau = \arctan \frac{\text{sign}(\sigma)\|\sigma\|_2}{\delta_0}. \quad (\text{II.26})$$

This tracking strategy is similar to that of [15], and is visualized in Figure 4.

E. Benchmark Controller

Since the safety controller derived in this paper considers worst-case environmental conditions, to alleviate conservatism we will activate it only when safety is at stake. Furthermore, the safety controller is only configured for the flight of the aircraft in the traction phase. To this end, we employ a primary controller synthesized using nonlinear dynamic inversion (NDI), an approach common in the aerospace sector [20]. For the NDI controller, we begin by calculating the optimal course and path angle rates ($\dot{\chi}_{\text{cmd}}$ and $\dot{\gamma}_{\text{cmd}}$) that lead to perfect curve tracking. Together with the course and path angle errors, we are able to compute the necessary pseudo-control inputs

$$v_{\chi} = \dot{\chi}_{\text{cmd}} + k_{p,\chi}(\chi_{\text{cmd}} - \chi) - \dot{\chi}_{\text{est}}, \quad (\text{II.27})$$

$$v_{\gamma} = \dot{\gamma}_{\text{cmd}} + k_{p,\gamma}(\gamma_{\text{cmd}} - \gamma) - \dot{\gamma}_{\text{est}}, \quad (\text{II.28})$$

where $k_{p,\chi}$ and $k_{p,\gamma}$ are control gains. Furthermore, $\dot{\chi}_{\text{est}}$ and $\dot{\gamma}_{\text{est}}$ are the estimated path angle rates based on a simplified version of the aircraft dynamics using a straight tether approximation, $\widehat{\mathbf{F}}_t$. Using the pseudo control inputs, we can construct the optimal control input, u_{NDI} , using the inverted aircraft dynamics. For detailed controller synthesis of the NDI controller, we refer to [8].

However, unlike in [8], we cannot assume perfect tension tracking. When the safety controller is activated, the tether tension will be reduced. We, therefore, update the simplified model of the NDI controller to use the true tether force, $\|\mathbf{F}_t\|_2$, projected along a straight line towards the origin. Thus the modified straight tether approximation is given by $\widehat{\mathbf{F}}_t = \frac{\mathbf{p}_{\text{aircraft}}}{\|\mathbf{p}_{\text{aircraft}}\|_2} \|\mathbf{F}_t\|_2$, where $\mathbf{p}_{\text{aircraft}}$ is the position of the aircraft, and \mathbf{F}_t is given by $\mathbf{F}_{s,n+1}$ as in (II.14).

III. Model Abstraction and Safety Considerations

For the derivation of the safety controller presented in Section IV, the previously introduced model does not suffice, since it requires too many states for synthesis. We thus begin by introducing a simplification of the tether model that allows us to introduce adversarial winch control into the AWE dynamics. Together with a new reference frame and the subsequent safety control model, this section provides the first of our four key contributions.

A. Simplified Tether Model

As mentioned in the previous sections, a full particle tether model requires too many states, prohibiting its adoption for the safety controller. From field tests conducted with an aircraft in [15], for a small aircraft the tether forces far exceed the gravitational forces and a straight tether approximation is reasonable. However, if larger systems with larger tethers are employed, the tether sag will need to be taken into account. For the AWE system considered in this paper, for the purpose of controller synthesis, we assume that the tether sag remains negligible and, therefore, opt to approximate the position and velocity of the tether segments. To this end, we assume that the position and velocity of the tether

segments are distributed evenly along a straight line between the origin and the position of the aircraft. Thus the tether particle's position and velocity can be computed as the x, y, and z projections of the straight tether up to the i-th particle, i.e.,

$$\mathbf{p}_i = \frac{i h_\tau}{n+1} \begin{bmatrix} \cos(\phi) \cos(\lambda) \\ \cos(\phi) \sin(\lambda) \\ \sin(\phi) \end{bmatrix}, \quad (\text{III.1})$$

$$\mathbf{v}_i = \frac{i \dot{h}_\tau}{n+1} \begin{bmatrix} \cos(\phi) \cos(\lambda) \\ \cos(\phi) \sin(\lambda) \\ \sin(\phi) \end{bmatrix} - \frac{i h_\tau}{n+1} \begin{bmatrix} \sin(\phi) \dot{\phi} \cos(\lambda) + \cos(\phi) \sin(\lambda) \dot{\lambda} \\ \sin(\phi) \dot{\phi} \sin(\lambda) - \cos(\phi) \cos(\lambda) \dot{\lambda} \\ -\cos(\phi) \dot{\phi} \end{bmatrix}. \quad (\text{III.2})$$

In Figure 3 a comparison of the straight tether and the full tether model is shown. Recall that the tether force acting on the aircraft is given by the spring force of the (n+1)-th segment, i.e., $\mathbf{F}_t = \mathbf{F}_{s,n+1}$. The dominating factor in Hooke's law is given by the term $\|\mathbf{s}_{n+1}\|_2 - l_s$, which is the difference between the segment length and the distance between the final tether point mass and the aircraft. Having $\|\mathbf{s}_{n+1}\|_2 - l_s > 0$ implies the distance is greater than the length of the tether and thus the tether is under tension. Modeling this term accurately is imperative for calculating the tether force, as the slightest deviations result in vastly inaccurate force calculations. To this end, let us introduce $\Delta_t = \|\mathbf{s}_{n+1}\|_2 - l_s$ as an additional state. By (II.14), the tether force acting on the aircraft can be calculated as

$$\mathbf{F}_t = \left(k \Delta_t + c \left(\frac{\mathbf{s}_{n+1}}{\|\mathbf{s}_{n+1}\|_2} \mathbf{s}_{v,n+1} \right) \right) \frac{\mathbf{s}_{n+1}}{\|\mathbf{s}_{n+1}\|_2}, \quad (\text{III.3})$$

where the position and velocity of the tether point masses is computed using (III.2).

The derivative of Δ_t is then given by

$$\dot{\Delta}_t = \frac{\mathbf{s}_{v,n+1}^T \mathbf{s}_{n+1}}{\|\mathbf{s}_{n+1}\|_2} - \frac{r_w \dot{\theta}_w}{n+1}, \quad (\text{III.4})$$

where \dot{l}_s , the reel-out speed of the tether, is substituted according to the winch dynamics (II.7). In order to keep the number of system states minimal, we need to decouple the winch system from the aircraft dynamics. To this end, we model the effects of the winch as a scalar disturbance, $d_{\Delta_t} := \dot{\Delta}_t$. By accounting for worst-case winch behavior, the system can be considered robust to arbitrary winch control. To compute the expected range of values that the derivative of Δ_t might take, we run a simulation of the AWE simulation using the baseline controller, introduced previously.

In Figure 5, $\dot{\Delta}_t$ for the traction phase of flight is shown. Since $\dot{\Delta}_t$ never exceeds $0.0015 \frac{m}{s}$, we constrain the disturbance, d_{Δ_t} , to lie within the interval $[-d_{\Delta_t, \max}, d_{\Delta_t, \max}]$ with $d_{\Delta_t, \max} = 0.005 \frac{m}{s}$.

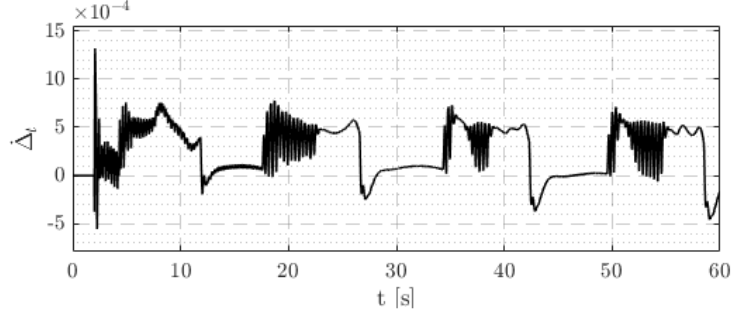


Fig. 5 $\dot{\Delta}_r$ during the traction phase of flight, using the baseline NDI controller.

B. Adversarial Wind Turbulence

Since we model the wind turbulence as a stochastic process, we need to ensure that the safety controller can account for worst-case wind gusts, i.e., wind gusts that drive the system away from its target trajectory, and/or lead to a tether rupture. To this end, we model the wind turbulence as an adversarial disturbance input to the system. Thus the wind velocity for controller synthesis is given by

$$(\mathbf{v}_W)_O = (\mathbf{v}_{\text{shear}})_O + (\mathbf{d}_{\text{turb}})_O, \quad (\text{III.5})$$

where $\mathbf{d}_{\text{shear}} \in \mathbb{R}^3$ is an additional disturbance vector

Similar to how we computed the bounds for d_{Δ_r} , we simulate the flight of the aircraft using the baseline controller and analyze the behavior of u_g , v_g and w_g . The wind gusts are shown in Figure 6. From the behaviour u_g , v_g and w_g , we can safely choose each element of \mathbf{d}_{turb} to be bounded by $\pm 4 \frac{m}{s}$.

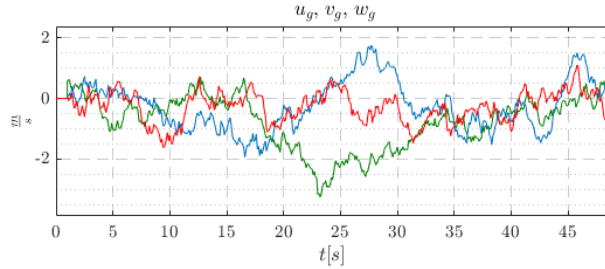


Fig. 6 The behavior of the wind gusts during 50 seconds of flight.

C. Γ Frame and Safety Control Model

As visualized in Figure 7, the geodesic vector pointing from \mathbf{C} along the geodesic towards \mathbf{K} , is always orthogonal to \mathbf{t} . The derivative of Γ together with the direction of the geodesic vector can, therefore, be used as basis vectors to construct another reference frame that will become useful during gridding, as discussed in Section IV. This new reference frame will be referred to as the Γ frame. Any point on \mathbb{S}^2 defined using the longitude λ and latitude ϕ can

dynamics serves both the presentation of the final system dynamics, as well as the derivation of the Hamiltonian in the subsequent section. Since the control inputs affect only the aircraft velocity, course, and path angles, with a slight abuse of notation, we omit the four remaining states derivatives that are zero, allowing us to summarize $\hat{\mathbf{f}}(\mathbf{x}, \mathbf{u})$ as

$$\hat{\mathbf{f}}(\mathbf{x}, \mathbf{u}) = \frac{1}{m_a} \begin{bmatrix} 1 & 0 & 0 \\ 0 & \frac{1}{v_a \cos \gamma_a} & 0 \\ 0 & 0 & -\frac{1}{v_a} \end{bmatrix} \mathbf{M}_{AA}^- \mathbf{M}_{AB} (\mathbf{F}_a)_B. \quad (\text{III.10})$$

The term $\mathbf{f}_C(\mathbf{x}, \mathbf{d})$ is then given by

$$\mathbf{f}_C(\mathbf{x}, \mathbf{d}) = \underbrace{\begin{bmatrix} \frac{(\mathbf{t})_\tau(\mathbf{v}_k)_\tau}{\|\mathbf{t}\|_2 l_\Gamma}, \frac{(\mathbf{t}_\perp)_\tau(\mathbf{v}_k)_\tau}{\|\mathbf{t}_\perp\|_2}, -(v_k)_{\tau,z}, \frac{(F_t)_{\bar{A},x}}{m_a}, \frac{(F_t)_{\bar{A},y}}{m_a v_a \cos \gamma_a}, -\frac{(F_t)_{\bar{A},z}}{m_a v_a}, 0 \end{bmatrix}^T}_{=\mathbf{f}_{C1}(\mathbf{x}, \mathbf{d}_{\text{turb}})} \quad (\text{III.11})$$

$$+ \underbrace{\begin{bmatrix} 0, 0, 0, 0, 0, 0, d_{\Delta_t} \end{bmatrix}^T}_{=\mathbf{f}_{C2}(\mathbf{x}, d_{\Delta_t})} \quad (\text{III.12})$$

$$+ \underbrace{\begin{bmatrix} 0, 0, 0, \frac{(F_g)_{\bar{A},x}}{m_a}, \frac{(F_g)_{\bar{A},y}}{m_a v_a \cos \gamma_a}, -\frac{(F_g)_{\bar{A},z}}{m_a v_a}, 0 \end{bmatrix}^T}_{=\mathbf{f}_{C3}(\mathbf{x})}, \quad (\text{III.13})$$

where we adopt the same notation as before to denote the x, y, and z components of the forces in the \bar{A} frame and simplify the notation by omitting the dependence of \mathbf{d}_{turb} and \mathbf{x} in the tether and gravitational forces.

IV. HJ Reachability Analysis and Controller Synthesis

A. Problem Statement

Having formulated the system dynamics, we are able to introduce the necessary concepts of HJ reachability analysis used for controller synthesis. The synthesized controller and subsequent hybrid control laws provide the second key contribution of this paper.

Let \mathcal{R} be the reach set, the set of states that should be reached in a given time, and let \mathcal{A} be the set of avoid states, the set of states that lead to a critical system failure (i.e., tether rupture). Then we can define the backward reachable set (BRS) as the set of states from which it is possible to reach the set \mathcal{R} at the end of a given time interval with duration T while guaranteeing never to enter the set \mathcal{A} until then. Mathematically, let $\mathbf{x} \in \mathbb{R}^7$ be the system state defined in (III.8) evolving according to the ordinary differential equation

$$\dot{\mathbf{x}}(t) = \mathbf{f}(\mathbf{x}(t), \mathbf{u}(t), \mathbf{d}(t)), \quad t \in [-T, 0], \mathbf{u} \in \mathcal{U}, \mathbf{d} \in \mathcal{D}. \quad (\text{IV.1})$$

Note that we treat time as negative consistent with [9, 22]; this only simplifies some of the notation and implies that we start our system at time $-T$. The dynamics, \mathbf{f} , are assumed to be bounded and Lipschitz continuous in \mathbf{x} and uniformly continuous in \mathbf{u} and \mathbf{d} . Then, given the Lebesgue-measurable functions $\mathbf{u}(\cdot) \in \mathcal{U}$ and $\mathbf{d}(\cdot) \in \mathcal{D}$, the control and disturbance inputs, respectively, there exists a unique trajectory, ζ , solving (IV.1), i.e.,

$$\begin{aligned} \frac{\partial}{\partial t} \zeta(t; \mathbf{x}_0, \mathbf{u}(\cdot), \mathbf{d}(\cdot)) &= \mathbf{f}(\zeta(t; \mathbf{x}_0, \mathbf{u}(\cdot), \mathbf{d}(\cdot)), \mathbf{u}(t), \mathbf{d}(t)), \forall t \in [-T, 0] \\ \zeta(-T; \mathbf{x}_0, \mathbf{u}(\cdot), \mathbf{d}(\cdot)) &= \mathbf{x}_0. \end{aligned}$$

To capture the worst-case disturbance, we model the underlying control problem as a differential game of two players. Following [23], we restrict the first player to play a nonanticipative strategy [24, 25], which is a function $\xi : \mathcal{D} \rightarrow \mathcal{U}$, such that for all $t \in [-T, 0]$ and for all $\mathbf{d}, \hat{\mathbf{d}} \in \mathcal{D}$, if $\mathbf{d}(\tau) = \hat{\mathbf{d}}(\tau)$ for almost every $\tau \in [-T, t]$, then $\xi[\mathbf{d}](\tau) = \xi[\hat{\mathbf{d}}](\tau)$ for almost every $\tau \in [-T, t]$. Furthermore, we use Σ to denote the class of nonanticipative strategies.

Finally, we can define the BRS as

$$\text{BRS}_{\mathcal{A}, \mathcal{R}}(-T) = \left\{ \mathbf{x} \in \mathbb{R}^7 \mid \exists \xi(\cdot) \in \Sigma, \forall \mathbf{d}(\cdot) \in \mathcal{D}, (\zeta(0; \mathbf{x}, \xi(\cdot), \mathbf{d}(\cdot)) \in \mathcal{R}) \ \& \ (\forall \tau \in [-T, 0], \zeta(\tau; \mathbf{x}, \xi(\cdot), \mathbf{d}(\cdot)) \notin \mathcal{A}) \right\}. \quad (\text{IV.2})$$

In words, $\text{BRS}_{\mathcal{A}, \mathcal{R}}(-T)$ is the set of states from which trajectories can start at $-T$, and there exists a choice for a non-anticipative strategy ξ , such that for any disturbance strategy \mathbf{d} , the system state can reach \mathcal{R} at the end of the horizon while avoiding \mathcal{A} until then.

By defining the avoid states as the set of states that imply a tether rupture, and the reach set as the set of states that follow the optimal guidance strategy, the BRS is able to provide information about an impending critical failure. Furthermore, by computing the BRS, we are able to simultaneously find the optimal trajectory and control policy that allows for optimal flight while avoiding critical states.

Recall that the maximum force acting on the tether is given by the final segment attached to the aircraft. Thus, by setting the maximum allowed tether force as F_{rupture} , we can define the Lipschitz continuous function $h(\mathbf{x}) = \|\mathbf{F}_t\|_2 - F_{\text{rupture}}$. Then we can define the avoid set related to the superzero level-set of $h(\cdot)$ as $\mathcal{A} = \{\mathbf{x} \in \mathbb{R}^7 \mid h(\mathbf{x}) > 0\}$.

Rather than defining our target set \mathcal{R} as being the set of states that lie on the optimal tracking curve, we define our target set as all states that are aligned with the commanded flight direction. To this end, we can define Lipschitz continuous function $l(\cdot)$ by taking the signed distance functions of the course and path errors in the NED frame $l(\mathbf{x}) = \max\{|\gamma_{\text{cmd}, O} - (\gamma)_O|, |\chi_{\text{cmd}, O} - (\chi)_O|\}$, where $(\gamma)_O$ and $(\chi)_O$ are the 5th and 6th states of our system transformed to the NED frame. The reach set is then defined by the subzero level-set of $l(\cdot)$, i.e., $\mathcal{R} = \{\mathbf{x} \in \mathbb{R}^7 \mid l(\mathbf{x}) \leq 0\}$.

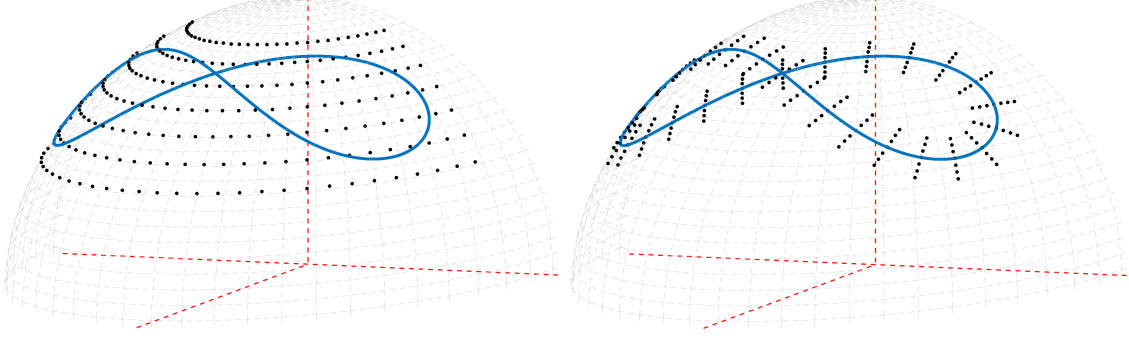


Fig. 8 Comparison of a 31×7 grid in the NED frame vs the Γ frame. The Γ frame successfully captures only relevant nodes close to the optimal tracking curve.

Using the definition of \mathcal{A} and \mathcal{R} , as in [23], it can be shown that $\text{BRS}_{\mathcal{A}, \mathcal{R}}(-T) = \{\mathbf{x} \in \mathbb{R}^7 | V(\mathbf{x}, T) \leq 0\}$, where

$$V(\mathbf{x}, t) = \inf_{\xi(\cdot) \in \Sigma} \sup_{\mathbf{d}(\cdot) \in \mathcal{D}} \max \left\{ l(\xi(0; \mathbf{x}, \xi(\cdot), \mathbf{d}(\cdot))), \max_{\tau \in [-t, 0]} h(\xi(\tau; \mathbf{x}, \xi(\cdot), \mathbf{d}(\cdot))) \right\}. \quad (\text{IV.3})$$

Furthermore, as in [22, 23], the value function in (IV.3) is the unique continuous viscosity solution of the following quasi-variational inequality

$$\max \left\{ h(\mathbf{x}) - V(\mathbf{x}, t), \frac{\partial V(\mathbf{x}, t)}{\partial t} + \sup_{\mathbf{d} \in D} \inf_{\mathbf{u} \in U} \frac{\partial V(\mathbf{x}, t)}{\partial \mathbf{x}} f(\mathbf{x}, \mathbf{u}, \mathbf{d}) \right\} = 0, \quad (\text{IV.4})$$

with terminal condition $V(\mathbf{x}, 0) = \max\{h(\mathbf{x}), l(\mathbf{x})\}$ and where D and U are the compact sets of possible disturbance and control inputs, respectively as defined in (III.9). For numerical reasons, it has become common practice to solve (IV.4) using level-set methods in combination with upwinding schemes such as essential non-oscillatory schemes [26]. Alternative methods for solving (IV.4), such as using Deep Learning [27] have been proposed, however, they lack many of the performance and safety guarantees we require.

To apply level-set methods to (IV.4), we are required to grid the state space, thus exponentially scaling the memory requirements with each additional state. This necessitates the need for the low dimensional model of the AWE system derived earlier in Section III. Furthermore, for each grid node, we are required to evaluate the dynamics and calculate the derivative of the value function. Therefore, to minimize computational overhead, we need to ensure we only consider grid nodes that are relevant during flight. To use conventional level-set methods, however, we are required to use an evenly spaced grid. As can be seen in Figure 8, gridding the position of the aircraft in the NED frame is inefficient compared to the new Γ frame introduced in Section III.C.

B. Optimal Control and Disturbance Inputs

To solve (IV.4), we are required to find the optimal control and disturbance inputs that are the minimizers and maximizers, respectively, of $\sup_{\mathbf{d} \in D} \inf_{\mathbf{u} \in U} \frac{\partial V(\mathbf{x}, t)}{\partial \mathbf{x}} \mathbf{f}(\mathbf{x}, \mathbf{u}, \mathbf{d})$. To this end let us define the Hamiltonian of the system as

$$H(\mathbf{x}, \mathbf{q}) = \max_{\mathbf{d} \in D} \min_{\mathbf{u} \in U} \mathbf{q}^T \mathbf{f}(\mathbf{x}, \mathbf{u}, \mathbf{d}), \quad (\text{IV.5})$$

where $\mathbf{q} = [q_1, \dots, q_7] \in \mathbb{R}^7$ is the costate vector and since both D and U are compact, we are able to define the Hamiltonian using the max and min over D and U , instead of the sup and inf, respectively, i.e., the optimizers are achieved. To determine the optimizers in (IV.5) we utilize the separation of the dynamics presented in Section III.C. This allows us to write the Hamiltonian as

$$H(\mathbf{x}, \mathbf{q}) = \min_{\mathbf{u} \in U} \mathbf{q}^T \hat{\mathbf{f}}(\mathbf{x}, \mathbf{u}) + \max_{\mathbf{d} \in D} \mathbf{q}^T \mathbf{f}_C(\mathbf{x}, \mathbf{d}), \quad (\text{IV.6})$$

separating the control from the disturbance inputs. We begin by finding the control inputs that minimize that Hamiltonian

$$\mathbf{u}^* \in \arg \min_{\mathbf{u} \in U} \mathbf{q}^T \hat{\mathbf{f}}(\mathbf{x}, \mathbf{u}) = \arg \min_{\mathbf{u} \in U} \frac{1}{m_a} \left[q_4 \left(\frac{q_5}{v_a \cos \gamma_a} - \frac{q_6}{v_a} \right) \mathbf{M}_{AA}^-(\mu) \mathbf{M}_{AB}(\alpha, \beta) (\mathbf{F}_a(\alpha, v_a))_B \right]. \quad (\text{IV.7})$$

No analytic expression for (IV.7) could be found, however, since we only need to know the optimal control inputs for a finite number of v_a, γ, q_4, q_5 , and q_6 values, we grid the input space and evaluate (IV.7) for discrete values of μ and α to find the near-optimal control inputs, i.e.,

$$\mathbf{u}^* \in \arg \min_{\alpha \in [\alpha_1, \dots, \alpha_n], \mu \in [\mu_1, \dots, \mu_m]} v_a q_4 (a(\alpha) \cos(\alpha) + b(\alpha) \sin(\alpha)) + \left(\frac{q_5}{\cos \gamma_a} \sin(\mu) + q_6 \cos(\mu) \right) (b(\alpha) \cos(\alpha) - a(\alpha) \sin(\alpha)), \quad (\text{IV.8})$$

where $a(\alpha)$ and $b(\alpha)$ are second order polynomials and $[\alpha_0, \dots, \alpha_n]$ and $[\mu_1, \dots, \mu_m]$ are discrete values of α and μ , respectively. Notice that u^* depends on the state implicitly through the costate vector q .

Determining the control inputs that minimize the Hamiltonian by means of (IV.8), we proceed to find the worst-case disturbances as the maximizer of the Hamiltonian, i.e., $\mathbf{d}^* \in \arg \max_{\mathbf{d} \in D} \mathbf{q}^T \mathbf{f}_C(\mathbf{x}, \mathbf{d}) = \arg \max_{d_{\Delta_t}, \mathbf{d}_{\text{turb}}} \mathbf{q}^T (\mathbf{f}_{C1}(\mathbf{x}, \mathbf{d}_{\text{turb}}) + \mathbf{f}_{C2}(\mathbf{x}, d_{\Delta_t}))$. Due to this separable structure, we begin by computing the worst case disturbance, d_{Δ_t} , which captures adverser winch control

$$d_{\Delta_t}^* \in \arg \max_{d_{\Delta_t} \in [-d_{\Delta_t, \max}, d_{\Delta_t, \max}]} \mathbf{q}^T \mathbf{f}_{C2}(\mathbf{x}, d_{\Delta_t}), \quad (\text{IV.9})$$

where $d_{\Delta_t, \max} = 0.005$ is considered the bound of $\dot{\Delta}_t$ as derived in Section III.A. Solving (IV.9) yields $d_{\Delta_t}^* = -\text{sign}(q_7) d_{\Delta_t, \max}$.

For the computation of the disturbance vector \mathbf{d}_{turb} , the worst case wind turbulence, we need to consider the effects

the wind turbulence has on the position and heading of the aircraft. The wind turbulence naturally influences the wind velocity (III.5) and subsequently the kinematic velocity of the aircraft (II.4). We thus begin by rewriting the kinematic velocity in the τ frame, whereby we replace the wind turbulence with the disturbance vector \mathbf{d}_{turb} , i.e.,

$$(\mathbf{v}_k)_\tau = \underbrace{\mathbf{M}_{\tau W} \mathbf{M}_{W O} \left(\mathbf{M}_{O \bar{A}} \begin{bmatrix} v_a \\ 0 \\ 0 \end{bmatrix}_{\bar{A}} + (\mathbf{v}_{\text{shear}})_O \right)}_{(\mathbf{v}_{k,0})_\tau} + \underbrace{\mathbf{M}_{\tau W} (\mathbf{d}_{\text{turb}})_W}_{(\mathbf{d}_{\text{turb}})_\tau}. \quad (\text{IV.10})$$

This allows us to rewrite the position propagation in the NED frame as

$$\dot{\lambda} = \underbrace{\frac{(v_{k,0})_{\tau,y}}{\cos(\phi)h_\tau}}_{\dot{\lambda}_0} + \frac{(d_{\text{turb}})_{\tau,y}}{\cos(\phi)h_\tau}, \quad (\text{IV.11})$$

$$\dot{\phi} = \underbrace{\frac{(v_{k,0})_{\tau,x}}{h_\tau}}_{\dot{\phi}_0} + \frac{(d_{\text{turb}})_{\tau,x}}{h_\tau}, \quad (\text{IV.12})$$

$$\dot{h}_\tau = \underbrace{-(v_{k,0})_{\tau,z}}_{\dot{h}_{\tau,0}} - (d_{\text{turb}})_{\tau,z}, \quad (\text{IV.13})$$

where $(v_{k,0})_{\tau,x}$, $(v_{k,0})_{\tau,y}$ and $(v_{k,0})_{\tau,z}$ denote the x, y, and z components of the base kinematic velocity in the τ frame and $(d_{\text{turb}})_{\tau,x}$, $(d_{\text{turb}})_{\tau,y}$ and $(d_{\text{turb}})_{\tau,z}$ denote the x, y and z components of the turbulence disturbance vector in the τ frame.

Recall that the tether force (III.3) is also affected by the kinematic velocity of the aircraft through the difference between the velocity of the aircraft and the final tether segment, given by $\mathbf{s}_{v,n+1} = \mathbf{v}_{\text{aircraft}} - \mathbf{v}_n$. To this end, let us rewrite \mathbf{v}_i using (IV.11)-(IV.13), to illustrate the dependence on \mathbf{d}_{turb} ,

$$\begin{aligned} \mathbf{v}_i = & \frac{i\dot{h}_{\tau,0}}{n+1} \begin{bmatrix} \cos(\phi) \cos(\lambda) \\ \cos(\phi) \sin(\lambda) \\ \sin(\phi) \end{bmatrix} - \frac{i(d_{\text{turb}})_{\tau,z}}{n+1} \begin{bmatrix} \cos(\phi) \cos(\lambda) \\ \cos(\phi) \sin(\lambda) \\ \sin(\phi) \end{bmatrix} - \frac{ih_\tau}{n+1} \begin{bmatrix} \sin(\phi) \cos(\lambda)\dot{\phi}_0 + \cos(\phi) \sin(\lambda)\dot{\lambda}_0 \\ \sin(\phi) \sin(\lambda)\dot{\phi}_0 - \cos(\phi) \cos(\lambda)\dot{\lambda}_0 \\ -\cos(\phi)\dot{\phi}_0 \end{bmatrix} - \\ & \frac{i(d_{\text{turb}})_{\tau,x}}{n+1} \begin{bmatrix} \sin(\phi) \cos(\lambda) \\ \sin(\phi) \sin(\lambda) \\ -\cos(\phi) \end{bmatrix} - \frac{i(d_{\text{turb}})_{\tau,y}}{\cos(\phi)(n+1)} \begin{bmatrix} \cos(\phi) \sin(\lambda) \\ -\cos(\phi) \cos(\lambda) \\ 0 \end{bmatrix}. \quad (\text{IV.14}) \end{aligned}$$

Denoting the base difference (i.e., neglecting the the disturbance) as $\mathbf{s}_{v,n+1,0}$, we can now rewrite $\mathbf{s}_{v,n+1}$ as

$$\mathbf{s}_{v,n+1} = \mathbf{s}_{v,n+1,0} - \frac{(d_{\text{turb}})_{\tau,z}}{n+1} \begin{bmatrix} \cos(\phi) \cos(\lambda) \\ \cos(\phi) \sin(\lambda) \\ \sin(\phi) \end{bmatrix} - \frac{(d_{\text{turb}})_{\tau,x}}{n+1} \begin{bmatrix} \sin(\phi) \cos(\lambda) \\ \sin(\phi) \sin(\lambda) \\ -\cos(\phi) \end{bmatrix} - \frac{(d_{\text{turb}})_{\tau,y}}{\cos(\phi)(n+1)} \begin{bmatrix} \cos(\phi) \sin(\lambda) \\ -\cos(\phi) \cos(\lambda) \\ 0 \end{bmatrix}. \quad (\text{IV.15})$$

As can be seen, by choosing an n sufficiently large, the effect of the disturbance on the tether force becomes negligible and we only need to consider the effects on the position propagation. Thus the worst-case turbulence disturbance can be calculated by

$$\mathbf{d}_{\text{turb}}^* \in \arg \max_{\substack{d_{\text{turb},x} \in D_{\text{turb}}, \\ d_{\text{turb},y} \in D_{\text{turb}}, \\ d_{\text{turb},z} \in D_{\text{turb}}}} \left[q_1, q_2, q_3 \right] \left[\dot{\lambda}, \dot{\phi}, \dot{h}_\tau \right]^T, \quad (\text{IV.16})$$

where $D_{\text{turb}} = [-d_{\text{turb,max}}, d_{\text{turb,max}}]$, with $d_{\text{turb,max}} = 4 \frac{m}{s}$, the possible range of turbulence velocities. The results in (IV.11)-(IV.13) utilize the disturbance in the τ frame, while we require the final result to be in the wind frame. To this end, we transform $(\mathbf{d}_{\text{turb}})_\tau$ back into the wind frame and drop the additive term $(\mathbf{v}_{k,0})_\tau$, resulting in the final worst case turbulence disturbances that maximize the Hamiltonian

$$\begin{aligned} d_{\text{turb},x}^* &= -d_{\text{turb,max}} \cdot \text{sign} \left[\sin(\phi) \cos(\lambda) \left(q_1 \frac{(t)_{\tau,x}}{\|\mathbf{t}\|_2 l_\Gamma} + q_2 \frac{(t_\perp)_{\tau,x}}{\|\mathbf{t}_\perp\|_2} \right) + \sin(\lambda) \left(q_1 \frac{(t)_{\tau,y}}{\|\mathbf{t}\|_2 l_\Gamma} + q_2 \frac{(t_\perp)_{\tau,y}}{\|\mathbf{t}_\perp\|_2} \right) \right. \\ &\quad \left. + \cos(\phi) \cos(\lambda) \left(q_1 \frac{(t)_{\tau,z}}{\|\mathbf{t}\|_2 l_\Gamma} + q_2 \frac{(t_\perp)_{\tau,z}}{\|\mathbf{t}_\perp\|_2} - q_3 \right) \right], \\ d_{\text{turb},y}^* &= d_{\text{turb,max}} \cdot \text{sign} \left[-\sin(\phi) \sin(\lambda) \left(q_1 \frac{(t)_{\tau,x}}{\|\mathbf{t}\|_2 l_\Gamma} + q_2 \frac{(t_\perp)_{\tau,x}}{\|\mathbf{t}_\perp\|_2} \right) + \cos(\lambda) \left(q_1 \frac{(t)_{\tau,y}}{\|\mathbf{t}\|_2 l_\Gamma} + q_2 \frac{(t_\perp)_{\tau,y}}{\|\mathbf{t}_\perp\|_2} \right) \right. \\ &\quad \left. - \cos(\phi) \sin(\lambda) \left(q_1 \frac{(t)_{\tau,z}}{\|\mathbf{t}\|_2 l_\Gamma} + q_2 \frac{(t_\perp)_{\tau,z}}{\|\mathbf{t}_\perp\|_2} - q_3 \right) \right], \\ d_{\text{turb},z}^* &= d_{\text{turb,max}} \cdot \text{sign} \left[\cos(\phi) \left(q_1 \frac{(t)_{\tau,x}}{\|\mathbf{t}\|_2 l_\Gamma} + q_2 \frac{(t_\perp)_{\tau,x}}{\|\mathbf{t}_\perp\|_2} \right) - \sin(\phi) \left(q_1 \frac{(t)_{\tau,z}}{\|\mathbf{t}\|_2 l_\Gamma} + q_2 \frac{(t_\perp)_{\tau,z}}{\|\mathbf{t}_\perp\|_2} - q_3 \right) \right]. \end{aligned}$$

With both the worst-case disturbance and optimal control inputs computed, the Hamiltonian can be calculated. To solve (IV.4) we employ the Level Set Method toolbox of [28] and begin by initializing the value function at $t = 0$ with $V(\mathbf{x}, 0) = \max\{h(\mathbf{x}), l(\mathbf{x})\}$. As we solve the quasi-variational inequality (IV.4), we compute the optimal control inputs that form our control policy $\mathbf{u}(\mathbf{x}, t)$. The evolution of the value function over the time period $[-0.1s, 0s]$ is shown in Figure 9. Any state in the zero-sublevel set belongs to the BRS, i.e., the set of points that can reach \mathcal{R} while avoiding \mathcal{A} within t units of time.

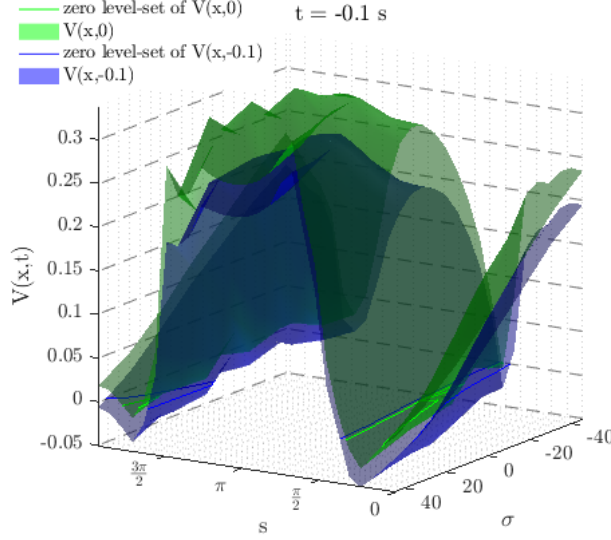


Fig. 9 Visualization of the value function used for safety controller synthesis projected along $[h_\tau = 250m, v_a = 31m/s, \chi_a = -0.4470, \gamma_a = 0.5205, \Delta_t = 0.0003m]$.

C. Hybrid Control Setup

Let us refer to the safety and the NDI control laws as u_{safety} and u_{NDI} respectively. Then we can introduce the following switching laws

$$S_1(\mathbf{F}_t) = (\|\mathbf{F}_t\|_2 \geq F_{\text{rupture}} - 30N) \quad \vee \quad (\|\mathbf{F}_t\|_2 + \frac{\partial \|\mathbf{F}_t\|_2}{\partial t} T \geq F_{\text{rupture}} - 50N), \quad (\text{IV.17})$$

$$S_2(\mathbf{F}_t) = \neg S_1(\|\mathbf{F}_t\|_2) \quad \wedge \quad \left[(\|\mathbf{F}_t\|_2 \leq F_{\text{rupture}} - 40N) \quad \vee \quad \left(\frac{\partial \|\mathbf{F}_t\|_2}{\partial t} \leq 0 \right) \right], \quad (\text{IV.18})$$

where $T = 0.1s$ is the time horizon used for the BRS computation and $\|\mathbf{F}_t\|_2$ is the moving average of the tether force acting on the aircraft. The switching law needs to be tuned for a given AWE setup and influences the trade-off between safety and conservatism. Since the actuation delays are not accounted for in the safety control synthesis, belated switching to the safety controller will potentially not give the safety controller ample time to take the necessary action to avoid a critical system failure. The switching law chosen in this work is based on the current tether force as well as a prediction of the expected tether force, however, further extensions can be made to include the BRS as a maneuverability envelope as in [29, 30]. The condition in IV.17 ensures that if the tether force comes within 30N of the critical force at which a rupture occurs, or, based on a linear extrapolation, the tether force will come within 50N of the critical tether force within the time horizon T , the safety controller will be activated. In turn, the condition IV.18 ensures that we only switch back to the NDI controller if the tether force is decreasing or we are below 40N of the critical rupture force, thus preventing bang-bang control. Using the switching laws, the applied control action is determined using a simple state automaton as illustrated in Figure 10.

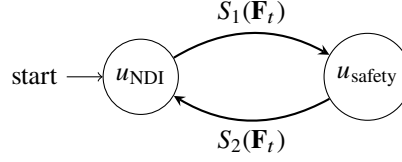


Fig. 10 State automaton of the hybrid control setup.

Table 1 Simulation Parameters

Parameter	Value	Description
F_{ref}	1600 N	Force tracked by the winch controller
F_{rupture}	1870 N	Force at which a tether rupture occurs
$ W_{20} $	$9 \frac{m}{s}$	Measured wind sped at 20 feet
ξ	π	Wind direction
n_{tether}	5	Tether segments used during simulation

V. Simulation

A. Simulation Setup

To simulate the full AWE setup, we extend the MATLAB Simulink framework presented in [8] and [7]. Together with the subsequent discussion, the validation of the presented hybrid control setup constitutes our fourth key contribution of this paper. Some of the relevant simulation parameters are presented in Table 1 and we have made the simulation code available in [31].

In order to accurately capture the behavior of the tether and thus detect a tether rupture, we simulate the tether dynamics using $n = 5$, i.e., 30 states. The winch is also simulated as a separate subsystem with a PI controller regulating the reel-in and reel-out speed of the winch. Both the aircraft and the tether are affected by wind shear, which is modeled using the MATLAB Aerospace Toolbox [16]. In addition to the wind shear, the aircraft is also subject to wind turbulence, which is modeled using the continuous Dryden turbulence block [16].

The aircraft dynamics use the tether force computed by the full tether model as well as the wind velocity computed by the wind field model. To this end, we pass the altitude of the aircraft and the tether segments to the wind field model. Since the aircraft model simulates the dynamics using the τ and the A frame, we need to convert the aircraft's longitude and latitude to the Γ frame before computing the safety control input. We, therefore, add a Navigator module that does the necessary frame transformations. Furthermore, we use the Navigator module to compute optimal course and path angle rates $\dot{\chi}_{\text{cmd}}$ and $\dot{\gamma}_{\text{cmd}}$, respectively. The course and path angle rates are then used by the NDI controller to compute the pseudo control inputs v_{χ} and v_{γ} based on the simplified aircraft dynamics.

To acquire the safety control inputs, u_{safety} , we solve (IV.8) using the numerically computed $\frac{\partial V(\mathbf{x}, T)}{\partial \mathbf{x}}$ as our costate vector. Since calculating the derivatives of the value function is computationally intensive, it is impractical to compute u_{safety} during the simulation. To this end, we calculate the optimal safety control inputs offline using a high fidelity grid

and save them on each grid point, using the saved values as a lookup table to be used during simulation.

Both control inputs, u_{safety} and u_{NDI} are passed to the control switch, which determines which control input to use based on the switching law derived in Section IV.C. The final control u_{cmd} is passed to the actuator, which simulates the actuator delays. The bank angle μ_a and angle of attack α_a are then passed to the aircraft model. To determine when to switch from traction to the retraction phase, we utilize the state machine, derived in [8].

B. Simulation Results

To evaluate the performance of the safety controller, we run the simulation for multiple pumping cycles to determine if, at any point, the maximum allowed tether force is exceeded. The tether force of three pumping cycles as well as the switching behavior of the safety controller is shown in Figure 11. Notice how the tether force is able to remain high throughout the pumping cycle and only minimal interventions by the safety controller (blue segments in the right image of Figure 11) are necessary to prevent a tether rupture.

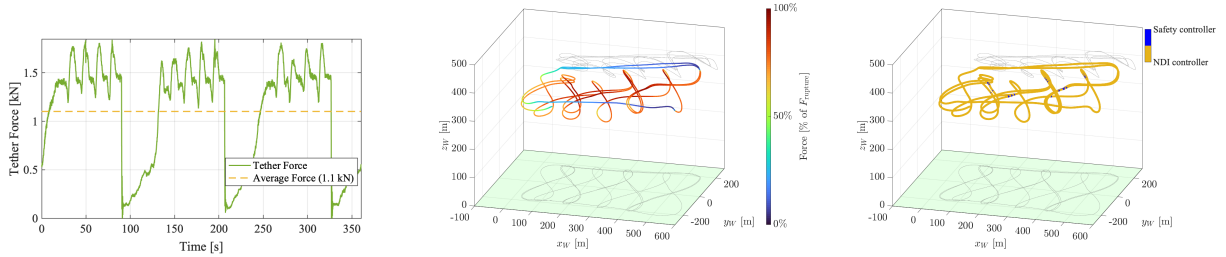


Fig. 11 (left) The tensile force of the tether acting on the aircraft during flight. (center) The tether force in % of the maximum allowed tether force before a rupture occurs. (right) The safety controller only needs to be activated at particular times. For the remainder of the flight, a more power-optimal controller, such as the NDI controller can be employed.

The power that is able to be harnessed by the ground station can be calculated by multiplying the tether force at the ground station by the reel-out speed, i.e., $P_{\text{mech}} = \dot{\theta}_w ||\mathbf{F}_w||_2$. In Figure 12, the power generation capabilities of the AWE system are shown. On average the chosen setup is able to produce 3.37 kW of power.

To put the power generation into context, we derive a theoretical upper limit of the power that could be obtained through optimal flight based on the work of [32]. We begin by calculating the maximum power harvesting factor, ζ , based on the drag and lift coefficients presented in [19]. The power harvesting factor is a common metric used by both AWE applications as well as conventional wind turbines (not to be confused with the power coefficient commonly used for wind turbines)

$$\zeta = \frac{4}{27} \frac{C_L^3}{(C_D + C_{D_{\text{tether}}})^2}. \quad (\text{V.1})$$

The power harvesting factor is unique for a given AWE setup and is used in [18] and [33] to calculate the theoretical limit P_{max} . However, in order to calculate a tighter, more realistic upper bounds of the power that a given controller

could achieve, we calculate an efficiency factor e that can be multiplied by the theoretical upper bound of the power generation, P_{\max} . This theoretical upper bound is given by Theorem 1 in [32], $\tilde{P} = P_{\max} \underbrace{\cos^3(\gamma_0)}_e$, where γ_0 is the optimal angle between the aerodynamic force and the wind.

Based on the observation that the average aerodynamic force needs to balance the gravitational force acting on the aircraft as well as the force exerted on the aircraft by the tether (assuming that on average the system is not accelerating), we can state the following equality based on a 2-dimensional simplification

$$\|\mathbf{F}_a\|_2 \begin{bmatrix} \cos \gamma_0 \\ \sin \gamma_0 \end{bmatrix} - \|\mathbf{F}_t\|_2 \begin{bmatrix} \cos \psi \\ \sin \psi \end{bmatrix} + \begin{bmatrix} \|\mathbf{F}_{\text{drag}}\|_2 \\ \|\mathbf{F}_g\|_2 \end{bmatrix} = 0, \quad (\text{V.2})$$

where ψ is the angle between the tether and the ground and $\|\mathbf{F}_{\text{drag}}\|_2$ is the negated x component of the aerodynamic force, $(\mathbf{F}_a)_A$. On average, ψ is equal to the rotation of the tracking curve, i.e., $\psi = \psi_0$.

As in [32], we multiply both sides by $[\sin \psi, -\cos \psi]^T$, which cancels out the effect of the tether, allowing us to solve for γ_0 , which in turn leads to the theoretical efficiency factor

$$e = \cos^3 \left(\psi_0 + \sin^{-1} \left(\frac{\|\mathbf{F}_{\text{drag}}\|_2}{\|\mathbf{F}_a\|_2} \sin \psi_0 + \frac{\|\mathbf{F}_g\|_2}{\|\mathbf{F}_a\|_2} \cos \psi_0 \right) \right). \quad (\text{V.3})$$

Finally, we calculate the theoretical maximum power that the hybrid control setup could obtain as

$$\tilde{P} = e A_{\text{eff}} \zeta \frac{1}{2} \rho \|\mathbf{v}_w\|_2^3. \quad (\text{V.4})$$

When evaluated and averaged, this equates to a theoretical average power of 5.56 kW. Thus the hybrid control setup comes close to the upper bound that could be achieved.

VI. Conclusion

We introduce a novel safety controller by deriving a low-dimensional simplification of the dynamics of an AWE system and applying HJ reachability analysis. By introducing switching conditions, the safety controller can be used in conjuncture with arbitrary controllers for safe and power-optimal flight. The hybrid control setup is simulated using a turbulence and wind shear model as well as actuation delays to simulate real-world environmental conditions. Using the hybrid control setup, we were able to successfully avoid a critical tether rupture while maintaining an average power output at a desired level. Future work will focus on improving the switching conditions between the safety controller and the NDI controller as well as incorporating actuator delays into the safety control framework.

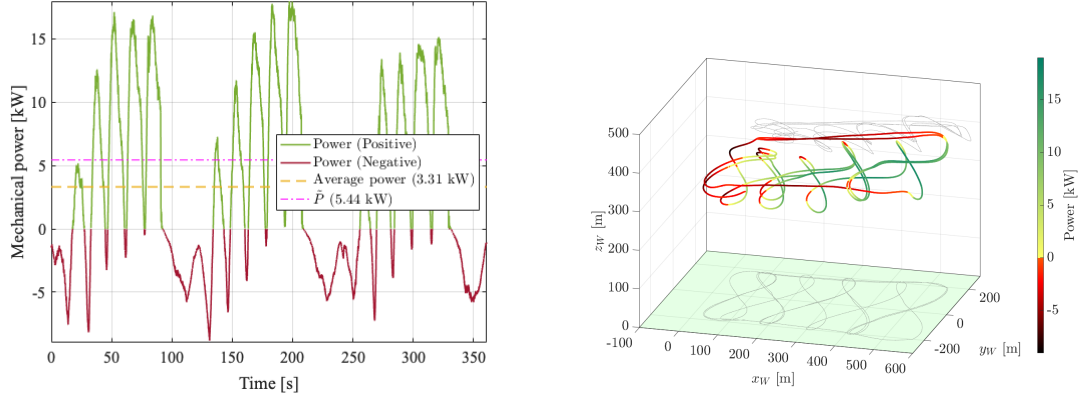


Fig. 12 (left) The power P_{mech} that is generated at the ground station during flight. (right) Generated power at the ground station in relation to the aircraft's flight path. The segments of negative power indicate a reeling in by the winch controller, i.e., the winch controller needs to exert power, while the yellow and green segments indicate the segments in which the winch controller is able to harvest power from the system.

Appendix

Coordinate transformation matrices

For brevity, we only list the transformation matrices in one direction, as the inverse transformation is obtained by simply transposing the appropriate matrix, since all transformation matrices are orthogonal [34].

$$\mathbf{M}_{AB} = \begin{bmatrix} \cos \alpha_a \cos \beta_a & \sin \beta_a & \sin \alpha_a \cos \beta_a \\ -\cos \alpha_a \sin \beta_a & \cos \beta_a & -\sin \alpha_a \sin \beta_a \\ -\sin \alpha_a & 0 & \cos \alpha_a \end{bmatrix}, \quad \mathbf{M}_{\tau W} = \begin{bmatrix} -\sin \phi \cos \lambda & -\sin \phi \sin \lambda & \cos \phi \\ -\sin \lambda & \cos \lambda & 0 \\ -\cos \phi \cos \lambda & -\cos \phi \sin \lambda & -\sin \phi \end{bmatrix}, \quad (\text{VI.1})$$

$$\mathbf{M}_{OW} = \begin{bmatrix} \cos \xi & \sin \xi & 0 \\ \sin \xi & -\cos \xi & 0 \\ 0 & 0 & -1 \end{bmatrix}, \quad \mathbf{M}_{AA} = \begin{bmatrix} 1 & 0 & 0 \\ 0 & \cos \mu_a & -\sin \mu_a \\ 0 & \sin \mu_a & \cos \mu_a \end{bmatrix}, \quad \mathbf{M}_{AO} = \begin{bmatrix} \cos \chi_a \cos \gamma_a & \sin \chi_a \cos \gamma_a & -\sin \gamma_a \\ -\sin \chi_a & \cos \chi_a & 0 \\ \cos \chi_a \sin \gamma_a & \sin \chi_a \sin \gamma_a & \cos \gamma_a \end{bmatrix}. \quad (\text{VI.2})$$

Acknowledgments

The authors would like to acknowledge Dr. Sebastian Rapp, Dylan Eijkelhof, and Prof. Roland Schmehl for making their simulation framework available.

References

- [1] IEA, "Wind Power," , November 2021. URL <https://www.iea.org/reports/wind-power>.

- [2] Schmehl, R., *Airborne Wind Energy: Advances in Technology Development and Research*, Springer, Singapore, 2018.
- [3] Commission, E., for Research, D.-G., and Innovation, *Study on challenges in the commercialisation of airborne wind energy systems*, Publications Office, 2018. <https://doi.org/doi/10.2777/87591>.
- [4] Fagiano, L., Zraggen, A. U., Morari, M., and Khammash, M., “Automatic crosswind flight of tethered wings for airborne wind energy: Modeling, control design, and experimental results,” *IEEE Transactions on Control Systems Technology*, Vol. 22, No. 4, 2014, pp. 1433–1447. <https://doi.org/10.1109/TCST.2013.2279592>.
- [5] Cherubini, A., Papini, A., Vertechy, R., and Fontana, M., “Airborne Wind Energy Systems: A review of the technologies,” *Renewable and Sustainable Energy Reviews*, Vol. 51, 2015, pp. 1461–1476. <https://doi.org/10.1016/j.rser.2015.07.053>.
- [6] Vermillion, C., Cobb, M., Fagiano, L., Leuthold, R., Diehl, M., Smith, R. S., Wood, T. A., Rapp, S., Schmehl, R., Olinger, D., and Demetriou, M., “Electricity in the air: Insights from two decades of advanced control research and experimental flight testing of airborne wind energy systems,” *Annual Reviews in Control*, Vol. 52, 2021, pp. 330–357. <https://doi.org/https://doi.org/10.1016/j.arcontrol.2021.03.002>.
- [7] Eijkelhof, D., Rapp, S., Fasel, U., Gaunaa, M., and Schmehl, R., “Reference Design and Simulation Framework of a Multi-Megawatt Airborne Wind Energy System,” *Journal of Physics: Conference Series*, Vol. 1618, No. 3, 2020. <https://doi.org/10.1088/1742-6596/1618/3/032020>.
- [8] Rapp, S., “Robust Automatic Pumping Cycle Operation of Airborne Wind Energy Systems Rapp,” Ph.D. thesis, Delft University of Technology, 2021. <https://doi.org/https://doi.org/10.4233/uuid:ab2adf33-ef5d-413c-b403-2cfb4f9b6bae>.
- [9] Bansal, S., Chen, M., Herbert, S., and Tomlin, C. J., “Hamilton-Jacobi reachability: A brief overview and recent advances,” *2017 IEEE 56th Annual Conference on Decision and Control (CDC)*, 2017, pp. 2242–2253. <https://doi.org/10.1109/CDC.2017.8263977>.
- [10] Vertovec, N., Ober-Blöbaum, S., and Margellos, K., “Multi-objective minimum time optimal control for low-thrust trajectory design,” *2021 European Control Conference (ECC)*, 2021, pp. 1975–1980. <https://doi.org/10.23919/ECC54610.2021.9654919>.
- [11] Chen, M., Herbert, S. L., Vashishtha, M. S., Bansal, S., and Tomlin, C. J., “Decomposition of Reachable Sets and Tubes for a Class of Nonlinear Systems,” *IEEE Transactions on Automatic Control*, Vol. 63, No. 11, 2018. <https://doi.org/10.1109/TAC.2018.2797194>.
- [12] Malz, E., Koenemann, J., Sieberling, S., and Gros, S., “A reference model for airborne wind energy systems for optimization and control,” *Renewable Energy*, Vol. 140, 2019, pp. 1004–1011. <https://doi.org/https://doi.org/10.1016/j.renene.2019.03.111>.
- [13] Rapp, S., and Schmehl, R., “Vertical takeoff and landing of flexible wing kite power systems,” *Journal of Guidance, Control, and Dynamics*, Vol. 41, No. 11, 2018, pp. 2386–2400. <https://doi.org/10.2514/1.G003535>.
- [14] Fechner, U., van der Vlugt, R., Schreuder, E., and Schmehl, R., “Dynamic model of a pumping kite power system,” *Renewable Energy*, Vol. 83, 2015, pp. 705–716. <https://doi.org/10.1016/j.renene.2015.04.028>.

- [15] Jehle, C., and Schmehl, R., “Applied tracking control for kite power systems,” *Journal of Guidance, Control, and Dynamics*, Vol. 37, No. 4, 2014, pp. 1211–1222. <https://doi.org/10.2514/1.62380>.
- [16] “MATLAB Aerospace Toolbox,” , 2021a. The MathWorks, Natick, MA, USA.
- [17] “U.S. Military Handbook MIL-HDBK-1797B,” , April 2012.
- [18] Diehl, M., “Airborne wind energy: Basic concepts and physical foundations,” *Airborne Wind Energy*, edited by U. Ahrens, M. Diehl, and R. Schmehl, Green Energy and Technology, Springer Berlin Heidelberg, Berlin, Heidelberg, 2013, pp. 3–22. <https://doi.org/10.1007/978-3-642-39965-7>.
- [19] Rapp, S., Schmehl, R., Oland, E., and Haas, T., “Cascaded pumping cycle control for rigid wing airborne wind energy systems,” *Journal of Guidance, Control, and Dynamics*, Vol. 42, No. 11, 2019, pp. 2456–2473. <https://doi.org/10.2514/1.G004246>.
- [20] Smith, P., “A simplified approach to nonlinear dynamic inversion based flight control,” 1998. <https://doi.org/10.2514/6.1998-4461>.
- [21] Chesler, P., “Numerical Solutions For Geodesics on Two Dimensional Surfaces,” , 1999.
- [22] Vertovec, N., Ober-Blöbaum, S., and Margellos, K., “Verification of safety critical control policies using kernel methods,” 2022 *European Control Conference (ECC)*, 2022, pp. 1870–1875. <https://doi.org/10.23919/ECC55457.2022.9838224>.
- [23] Margellos, K., and Lygeros, J., “Hamilton-jacobi formulation for reach-avoid differential games,” *IEEE Transactions on Automatic Control*, Vol. 56, No. 8, 2011, pp. 1849–1861. <https://doi.org/10.1109/TAC.2011.2105730>.
- [24] Varaiya, P. P., “On the Existence of Solutions to a Differential Game,” *SIAM Journal on Control*, Vol. 5, No. 1, 1967, pp. 153–162. <https://doi.org/10.1137/0305009>.
- [25] Evans, L., and Souganidis, P. E., “Differential games and representation formulas for solutions of Hamilton-Jacobi-Isaacs equations,” *Indiana Univ. Math. J.*, Vol. 33, No. 5, 1984, pp. 773–797.
- [26] Osher, S., and Fedkiw, R., *Level Set Methods and Dynamic Implicit Surfaces*, Applied Mathematical Sciences, Springer New York, 2003.
- [27] Bansal, S., and Tomlin, C., “DeepReach: A Deep Learning Approach to High-Dimensional Reachability,” , November 2020. URL <http://arxiv.org/abs/2011.02082>.
- [28] Mitchell, I. M., “The flexible, extensible and efficient toolbox of level set methods,” *Journal of Scientific Computing*, Vol. 35, No. 2-3, 2008, pp. 300–329. <https://doi.org/10.1007/s10915-007-9174-4>.
- [29] Fisac, J. F., Akametalu, A. K., Zeilinger, M. N., Kaynama, S., Gillula, J., and Tomlin, C. J., “A General Safety Framework for Learning-Based Control in Uncertain Robotic Systems,” *IEEE Transactions on Automatic Control*, Vol. 64, No. 7, 2019, pp. 2737–2752. <https://doi.org/10.1109/TAC.2018.2876389>.

- [30] Herbert, S., Choi, J. J., Sanjeev, S., Gibson, M., Sreenath, K., and Tomlin, C. J., “Scalable Learning of Safety Guarantees for Autonomous Systems using Hamilton-Jacobi Reachability,” *2021 IEEE International Conference on Robotics and Automation (ICRA)*, 2021, pp. 5914–5920. <https://doi.org/10.1109/ICRA48506.2021.9561561>.
- [31] Vertovec, N., 2022. URL https://github.com/nikover/AWE_Simulation.
- [32] Costello, S., Costello, C., François, G., and Bonvin, D., “Analysis of the maximum efficiency of kite-power systems,” *Journal of Renewable and Sustainable Energy*, Vol. 7, No. 5, 2015, pp. 1–16. <https://doi.org/10.1063/1.4931111>.
- [33] Loyd, M. L., “Crosswind Kite Power.” *Journal of energy*, Vol. 4, No. 3, 1980, pp. 106–111. <https://doi.org/10.2514/3.48021>.
- [34] Nair, M. T., and Singh, A., *Linear algebra*, Springer, Singapore, 2018.